PAPER

Effectively realizing broadband spectral conversion of UV/visible to near-infrared emission in (Na,K)Mg(La,Gd)TeO$_6$:Mn^{4+},Nd^{3+},Yb^{3+} materials for c-Si solar cells *via* efficient energy transfer†

Kai Li (iD) * and Rik Van Deun (iD) *

In this work, a series of (Na,K)Mg(La,Gd)TeO$_6$:Mn^{4+},Nd^{3+},Yb^{3+} materials were prepared *via* a high-temperature solid-state reaction method. As reported before, certain Mn^{4+} singly doped samples present good red luminescence properties, showing emission bands at around 700 nm upon excitation with UV/n-UV/blue light. When Mn^{4+} and Nd^{3+} were co-doped into the same host, effective energy transfer from Mn^{4+} to Nd^{3+} ions was inferred from the spectral overlap of the Mn^{4+} emission and Nd^{3+} excitation bands. The variation of the emission bands upon 365 nm UV excitation with fixed Mn^{4+} concentration and varying Nd^{3+} concentration in phosphors can validate this energy transfer process from Mn^{4+} to Nd^{3+} ions. In addition, comparison of the excitation spectra monitored at the Nd^{3+} emission peaks to those monitored at the Mn^{4+} emission bands and the decrease of the Mn^{4+} decay times supplied more evidence for the energy transfer phenomenon from Mn^{4+} to Nd^{3+} ions in these Mn^{4+},Nd^{3+} co-doped samples. Since the energy transfer from Nd^{3+} to Yb^{3+} ions has been well reported before, we co-doped Yb^{3+} in our Mn^{4+},Nd^{3+} co-doped samples to show that Nd^{3+} can be a bridging ion to regulate the energy transfer from Mn^{4+} to Yb^{3+} ions for the first time, which was confirmed from the analysis of the excitation spectra and decay times. This can be considered as a novel method to enhance the energy transfer from Mn^{4+} to Yb^{3+} ions. Based on the energy transfer from Mn^{4+} to Nd^{3+} and then to Yb^{3+}, UV/visible luminescence can be effectively converted into near-infrared emission, allowing a better spectral response for c-Si solar cells, which suggests a possible enhancement of the conversion efficiency of such c-Si solar cells.

1. Introduction

Considering the increasing global energy consumption, effectively utilizing solar energy has been adopted as an alternative approach to relieve the energy crisis since it is an inexhaustible and green energy for human beings; therefore, the relevant technologies of converting sunlight into electricity with solar cell devices have been developed for over half a century.[1–4] However, it still remains more expensive than conventional fossil fuels because of the low conversion efficiency of solar energy despite the great advances that have been made in the last few decades. Until now, crystalline Si (c-Si) solar cells have occupied the majority of the solar cell market owing to their well-developed techniques and low cost. B. Richard *etc.* and T. Trupke *etc.* predicted that the theoretical maximum value of

the conversion efficiency for crystalline Si (c-Si) solar cells could exceed 30% several years ago,[5,6] whereas the values of the conversion efficiency for laboratory and commercial application are only about 25% and 22% currently, respectively.[7] The essential issue for restricting the energy conversion efficiency primarily originates from the mismatch between the energy distribution of the incident sunlight spectrum and the energy gap of the c-Si semiconductor material, which means that incident photons with energy lower than the band gap of the c-Si material cannot be absorbed and the excessive energy for photons with energy higher than the band gap will be released in the form of heat to cause thermalization losses.[8,9] It is well known that the current c-Si solar cells have their maximum spectral response in the narrow band range of 900–1100 nm, matching their energy gap, while the total energy for this range is only a fraction of the whole solar spectrum, as most of the energy of the solar spectrum is concentrated at wavelengths beyond 900 nm.[10] Consequently, reducing the energy loss of this part *via* spectral converters is an important alternative approach to improve the energy conversion efficiency of c-Si

L³ – Luminescent Lanthanide Lab, Department of Chemistry, Ghent University, Krijgslaan 281-S3, B-9000 Ghent, Belgium. E-mail: kailiciac@126.com, Rik.VanDeun@UGent.be

† Electronic supplementary information (ESI) available. See DOI: 10.1039/c8tc02019a

7302 | *J. Mater. Chem. C*, 2018, **6**, 7302–7310

This journal is © The Royal Society of Chemistry 2018

solar cells.[11] As shown in Fig. S1 (ESI†), a simple c-Si solar cell device model consists of several parts, and the spectral conversion materials are generally coated on the anti-reflection (AR) coating layer, which can convert UV/invisible light into NIR photons absorbed by the c-Si solar cells.[12]

Lanthanide ions, often having a rich energy level structure, can be used to get near-infrared (NIR) luminescent materials,[13–15] of which Yb^{3+} and Nd^{3+} are considered to be the two most ideal activators for photovoltaic applications because the Yb^{3+} NIR emission around 1000 nm (attributed to the $^2F_{5/2} \rightarrow {}^2F_{7/2}$ transition) is just above the edge of c-Si, and the Nd^{3+} NIR emission around 1064 nm (attributed to the $^4F_{3/2} \rightarrow {}^4I_{11/2}$ transition) can match well with the spectral response of the c-Si semiconductor material.[16] However, lanthanides exhibit weak and narrow excitation bands originating from their parity-forbidden 4f–4f transitions, which result in the conversion of only a small part of UV and visible sunlight to NIR light. Therefore, co-doping a suitable sensitizer to absorb UV/visible light is an effective approach to enhance the conversion efficiency of UV/visible light to NIR emission *via* an efficient energy transfer process. Many systems such as Tm^{3+}–Yb^{3+}, Ce^{3+}–Yb^{3+}, Eu^{2+}–Yb^{3+}, Ho^{3+}–Yb^{3+}, Bi^{3+}–Yb^{3+}, Cr^{3+}–Yb^{3+}, Yb^{2+}–Yb^{3+}, Ce^{3+}–Nd^{3+}, $(VO_4)^{3-}$–Nd^{3+}, Eu^{2+}–Nd^{3+}, and Cr^{3+}–Nd^{3+} have been investigated to realize this enhanced spectral conversion.[17–27] However, it is still a research hotspot to enhance the NIR emission of Nd^{3+}/Yb^{3+} with the excitation of UV/visible light in an environmentally-friendly host with excellent chemical, mechanical and thermal stabilities. In addition, as a transitional metal, tetravalent Mn^{4+} has attracted a lot of interest acting as an activator in red luminescent materials because its Mn^{4+}–O^{2-} charge transfer transition, and $^4A_2 \rightarrow {}^4T_1$ and $^4A_2 \rightarrow {}^4T_2$ d–d spin-allowed transitions show strong absorption in the UV and visible region. The resulting red or deep red luminescence within the 600–750 nm wavelength range is attributed to its $^2E_g \rightarrow {}^4A_{2g}$ transition, which indicates its possible use for broadband conversion as a sensitizer.[28] Hence, it was first reported as a possible sensitizer for Yb^{3+} in the $Ca_{14}Al_{10}Zn_6O_{35}$ host in 2016.[29] Recently, two La_2MgTiO_6:Mn^{4+},Yb^{3+} and Gd_2ZnTiO_6:Mn^{4+},Yb^{3+} systems have also been developed to illustrate the sensitization of Mn^{4+} for Yb^{3+} ions.[30,31] Generally, the energy transfer process from Mn^{4+} to Yb^{3+} ions would like to take place *via* a phonon-assisted non-resonant mechanism similar to Cr^{3+}, which requires several phonons to compensate for energy loss.[32,33] This may be attributed to the limited spectral overlap between them and the resulting low energy transfer effect. The Nd^{3+} ion has been reported as a good sensitizer to transfer its energy to Yb^{3+} ions in a variety of hosts.[34–37] Therefore, Nd^{3+} can be estimated to act as a bridging ion to enhance the energy transfer process from Mn^{4+} to Yb^{3+} since Mn^{4+} generally has a large spectral overlap with Nd^{3+}. This may lead to a better conversion efficiency of UV/visible to NIR emission with Mn^{4+} to Yb^{3+} ion and Nd^{3+} to Yb^{3+} ion energy transfer processes. Recently, we developed a novel series of Mn^{4+} doped $(Na,K)Mg(La,Gd)TeO_6$ phosphors showing excellent luminescence properties.[38,39] Based on the idea above, we have now synthesized a series of Mn^{4+}, Nd^{3+} and Yb^{3+} co-doped

$(Na,K)Mg(La,Gd)TeO_6$ phosphors using a high-temperature solid-state reaction method. A pure phase was obtained in all the as-prepared samples. The luminescence properties and energy transfer processes in these materials have been investigated in detail. We proposed that two Mn^{4+} ions would simultaneously replace one Mg^{2+} and one Te^{6+} ion, which are both coordinated by six oxygen atoms, to keep the charge balance.[38,39] This was proposed as a novel method to obtain red emitting Mn^{4+} doped phosphors. In these materials, La^{3+}/Gd^{3+} sites can be occupied by Yb^{3+} and Nd^{3+} ions because of their similar ionic radii. We found that a large spectral overlap between Mn^{4+} and Nd^{3+} ions occurs, resulting in efficient energy transfer from Mn^{4+} to Nd^{3+} ions. In addition, the energy transfer process of $Mn^{4+} \rightarrow Nd^{3+} \rightarrow Yb^{3+}$ was validated when co-doping Yb^{3+} into the Mn^{4+}–Nd^{3+} system. Therefore, it is rational to imply that Mn^{4+} can efficiently transfer its energy to Nd^{3+} and then to Yb^{3+}, which offers an attractive route to realize spectral conversion for enhancing the energy conversion efficiency of c-Si solar cells.

2. Synthesis and characterization of the materials

2.1 Synthesis of the materials

A series of polycrystalline powder samples of $(Na,K)Mg(La,Gd)TeO_6$:Mn^{4+},Nd^{3+},Yb^{3+} [$NaMgLa_{1-x-a}TeO_6$:$0.02Mn^{4+}$,xNd^{3+},aYb^{3+} (x = 0–0.04, a = 0–0.10), $NaMgGd_{1-y-b}TeO_6$:$0.01Mn^{4+}$,yNd^{3+},bYb^{3+} (y = 0–0.04, b = 0–0.30) and $KMgLa_{1-z-c}TeO_6$:$0.006Mn^{4+}$,zNd^{3+},cYb^{3+} (z = 0–0.04, c = 0–0.10), abbreviated as NML:$0.02Mn^{4+}$,xNd^{3+},aYb^{3+}, NMG:$0.01Mn^{4+}$,yNd^{3+},bYb^{3+} and KML:$0.006Mn^{4+}$,zNd^{3+},cYb^{3+}, respectively] were prepared *via* a high-temperature solid-state reaction method. Typically, raw materials containing Na_2CO_3 (AR), K_2CO_3 (AR), $(MgCO_3)_4 \cdot Mg(OH)_2 \cdot 5H_2O$ (AR), La_2O_3 (99.99%), Gd_2O_3 (99.99%), TeO_2 (99.99%), Yb_2O_3 (99.99%), $Nd(NO_3)_3 \cdot 6H_2O$ (99.99%) and $MnCO_3$ (99.99%) were first stoichiometrically weighed according to the required chemical formula, then mixed and ground for about 15 min in an agate mortar with a pestle after adding an appropriate amount of ethanol. The homogeneous mixtures needed another 1 min of grinding after drying in an oven and were then transferred to ceramic crucibles to anneal in a furnace at 1100 °C for 11 h with a heating rate of 10 °C min^{-1}. Finally, the products were cooled within the furnace and ground for 1 min for subsequent characterization.

2.2 Characterization

The phase purity of the as-prepared samples was characterized by Powder X-ray diffraction (PXRD) conducted on a Thermo Scientific ARLX'TRA diffractometer equipped with a Cu Kα (λ = 1.5405 Å) source, keeping the scan rate at 5° min^{-1} in the scattering angle range (2θ) of 15°–65°. Rietveld refinement of a PXRD profile needs the range to be 5°–90° with a scan rate of 0.5° min^{-1}. Photoluminescence (PL) spectra and luminescence lifetimes were measured on an Edinburgh Instruments FLSP 920 UV-vis-NIR spectrofluorimeter, equipped with a 450 W continuous xenon lamp and a 60 W pulsed xenon lamp. The setup has a Hamamatsu R928P red-sensitive photomultiplier tube (PMT) to

This journal is © The Royal Society of Chemistry 2018

J. Mater. Chem. C, 2018, **6**, 7302–7310 | 7303

detect luminescence in the 200–870 nm wavelength range, and a liquid-nitrogen cooled (−80 °C) Hamamatsu R5509-72 PMT to detect near-infrared luminescence up to 1700 nm. All the measurements were conducted at room temperature.

3. Results and discussion

Rietveld refinements for the NML, NML:0.02Mn^{4+},0.01Nd^{3+}, NMG, NMG:0.01Mn^{4+},0.012Nd^{3+}, KML and KML:0.006Mn^{4+}, 0.02Nd^{3+} samples were performed to identify the phase purities of the as-prepared samples using the General Structure Analysis System (GSAS) programme.[40] The results are plotted in Fig. 1a–f, respectively. The structure of the NaMgLaTeO$_6$ (ICSD 78532) compound was taken as the original structure mode for refinements. As seen in Fig. 1a–f, the magenta solid lines and red vertical bars represent the calculated patterns and Bragg diffraction positions from the NaMgLaTeO$_6$ structure, respectively. The black crosses show the experimental patterns and the green lines below the red bars illustrate the differences between the calculated and experimental results. It can be observed that all atom coordinates, fraction factors and thermal vibration parameters are in accordance with the reflection conditions, which can be implied from the R_{wp}, R_p and χ^2 values, as displayed in Fig. 1a–f, and which indicates the reliability of the refined results. Detailed cell parameters for these samples are listed in Table 1, in which
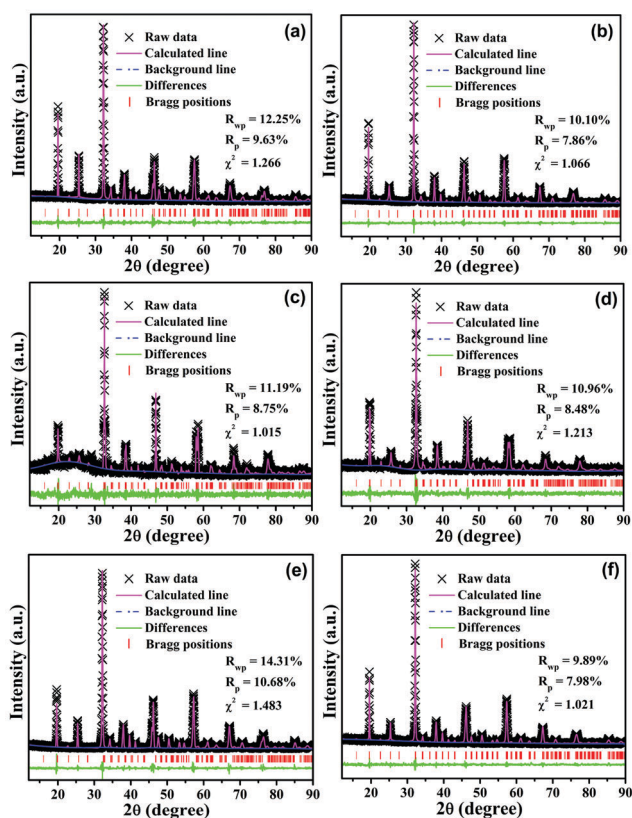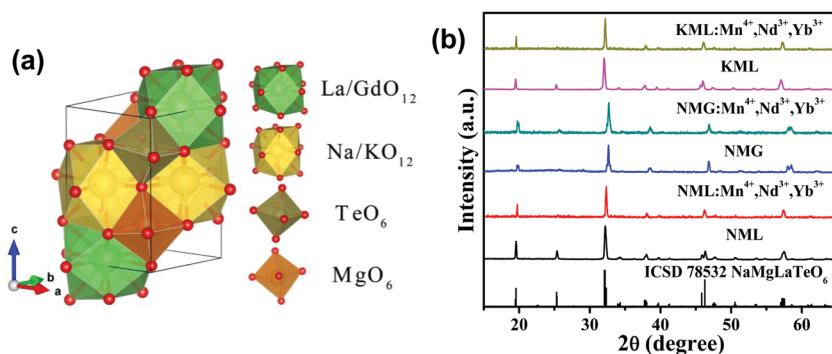
the variations of the cell parameters of the doped samples as compared to those of the hosts originate from the incorporation of the dopants. Therefore, it can be concluded that the NaMgGdTeO$_6$ and KMgLaTeO$_6$ compounds are isostructural with the NaMgLaTeO$_6$ compound, which crystallizes in a monoclinic system with a space group $P121/m1(11)$, as depicted in Fig. 2a. Both Mg and Te atoms locate at a six-fold site (2e) to form respective MgO$_6$ and TeO$_6$ octahedra with a shared oxygen atom. Moreover, La/Gd and Na/K atoms are coordinated with twelve oxygen atoms to form polyhedral La/GdO$_{12}$ and Na/KO$_{12}$. These four kinds of polyhedra connect closely to construct the space framework of this crystal structure. Therefore, red luminescence can be generated when Mn^{4+} ions substitute Mg^{2+} and Te^{6+} sites simultaneously to keep the charge balance, which has been demonstrated in our previous work.[38,39] Nd^{3+} and Yb^{3+} are proposed to occupy La^{3+} or Gd^{3+} sites because of their close ionic radii. Representative PXRD patterns of the host and of Mn^{4+},Nd^{3+},Yb^{3+} co-doped samples are shown in Fig. 2b. It illustrates that all the XRD patterns can be well assigned to the standard reference NaMgLaTeO$_6$ (ICSD 78532) compound, which further proves the pure phase of the as-prepared samples. The slight shift to larger angle observed by comparing doped and un-doped samples is ascribed to the substitution of Mn^{4+} for Mg^{2+} and Te^{6+} and Nd^{3+}/Yb^{3+} for La^{3+}/Gd^{3+}.
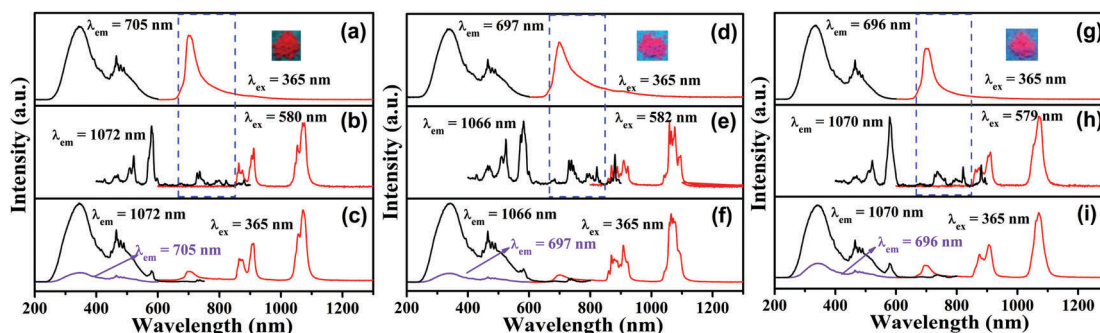
The PL excitation and emission spectra of NML:0.02Mn^{4+}, NML:0.02Nd^{3+}, and NML:0.02Mn^{4+},0.02Nd^{3+}, which are presented in Fig. 3a–c, respectively, serve as examples to show the spectral overlap between Mn^{4+} and Nd^{3+} ions and to demonstrate the energy transfer possibility from Mn^{4+} to Nd^{3+} ions. As displayed in Fig. 3a, Mn^{4+} doped NML shows a relatively narrow band from 600 nm to 1000 nm peaking at 705 nm upon 365 nm excitation. This corresponds to an intense red luminescence, as displayed in the inset of Fig. 3a, which is attributed to the Mn^{4+} transition $^2E_g \rightarrow {}^4A_{2g}$. Two Mn^{4+} ions are proposed to substitute Mg^{2+} and Te^{6+} ions simultaneously, based on the spectral analysis we reported before,[38,39] which provides an attractive idea to realize Mn^{4+} red luminescence by Mn^{4+} substitution for two different kinds of sites to keep the charge balance. Monitored at 705 nm, the excitation spectrum covers the UV to visible region with the range of 250–600 nm, which can be deconvoluted into four Gaussian bands peaking at 316 nm (31 645 cm^{-1}) from the Mn^{4+}–O^{2-} charge transfer transition, and 355 nm (28 169 cm^{-1}), 406 nm (24 631 cm^{-1}) and 478 nm (20 921 cm^{-1}) from the Mn^{4+} spin-allowed transitions $^4T_{1g} \leftarrow {}^4A_{2g}$, $^2T_{2g} \leftarrow {}^4A_{2g}$ and $^4T_{2g} \leftarrow {}^4A_{2g}$, respectively, as presented in Fig. S2a (ESI†). These results indicate that UV or visible light in the NML:Mn^{4+} system can be efficiently converted into red light. The PL emission spectrum of Nd^{3+} doped NML shows two main bands around 910 nm and 1072 nm under 580 nm excitation, as shown in Fig. 3b, corresponding to Nd^{3+} transitions $^4F_{3/2} \rightarrow {}^4I_{9/2}$ and $^4F_{3/2} \rightarrow {}^4I_{11/2}$, respectively.[41] The excitation spectrum monitored at 1072 nm consists of several narrow bands at around 470 nm, 509 nm, 522 nm, 580 nm, 597 nm, 672 nm, 736 nm, 800 nm and 880 nm in the range of 400–900 nm, which originate from the Nd^{3+} 4f–4f transitions (^{2}D,^{2}P)$_{3/2}$, ^{2}G$_{9/2}$, ^{2}K$_{15/2}$ ← ^{4}I$_{9/2}$, ^{4}G$_{9/2}$, ^{2}K$_{13/2}$ ← ^{4}I$_{9/2}$, ^{4}G$_{7/2}$ ← ^{4}I$_{9/2}$, ^{2}G$_{7/2}$, ^{4}G$_{5/2}$ ← ^{4}I$_{9/2}$, ^{2}H$_{11/2}$ ← ^{4}I$_{9/2}$,

Fig. 1 Rietveld refinements for the NML (a), NML:0.02Mn^{4+},0.01Nd^{3+} (b), NMG (c), NMG:0.01Mn^{4+},0.012Nd^{3+} (d), KML (e) and KML:0.006Mn^{4+}, 0.02Nd^{3+} (f) samples.

7304 | J. Mater. Chem. C, 2018, 6, 7302–7310

This journal is © The Royal Society of Chemistry 2018

Table 1 Crystallographic data and details in the data collection and refinement parameters for the NML host, NML:0.02Mn^{4+},0.01Nd^{3+}, the NMG host, NMG:0.01Mn^{4+},0.012Nd^{3+}, the KML host and KML:0.006Mn^{4+},0.02Nd^{3+} samples

Sample	NML	NML:0.02Mn^{4+},0.01Nd^{3+}	NMG	NMG:0.01Mn^{4+},0.012Nd^{3+}	KML	KML:0.006Mn^{4+},0.02Nd^{3+}
Space group	P121/m1	P121/m1	P121/m1	P121/m1	P121/m1	P121/m1
Symmetry	Monoclinic	Monoclinic	Monoclinic	Monoclinic	Monoclinic	Monoclinic
a, Å	5.5645(2)	5.5372(3)	5.5176(3)	5.5110(4)	5.5866(1)	5.5658(1)
b, Å	5.5491(3)	5.5458(2)	5.4479(3)	5.4511(4)	5.5751(3)	5.5468(3)
c, Å	7.8935(3)	7.9052(3)	7.7660 (4)	7.7514(3)	7.9530(3)	7.8951(3)
V, Å^3	243.73(2)	242.75(2)	233.44(2)	232.86(3)	247.70(2)	243.74(2)
Z	1	1	1	1	1	1
$\alpha = \gamma$, °	90	90	90	90	90	90
β, °	90.120(3)	89.970(4)	89.947(3)	89.821(5)	90.119(3)	90.122(3)
2θ-interval, °	5–90	5–90	5–90	5–90	5–90	5–90
R_{wp}/%	12.25%	10.10	11.19	10.96	14.31	9.89
R_{p}/%	9.63%	7.86	8.75	8.48	10.68	7.98
χ^2	1.266	1.066	1.015	1.213	1.483	1.021

Fig. 2 XRD patterns for the NML, NML:0.02Mn^{4+},0.01Nd^{3+},0.10Yb^{3+}, NMG, NMG:0.01Mn^{4+},0.02Nd^{3+},0.02Yb^{3+}, KML, KML:0.006Mn^{4+},0.03Nd^{3+},0.10Yb^{3+} samples as well as the standard diffraction positions of the reference compound NaMgLaTeO$_6$ (ICSD 78532).

Fig. 3 PL excitation and emission spectra of NML:0.02Mn^{4+} (a), NML:0.02Nd^{3+} (b), NML:0.02Mn^{4+},0.02Nd^{3+} (c), NMG:0.01Mn^{4+} (d), NMG:0.02Nd^{3+} (e), NMG:0.01Mn^{4+},0.02Nd^{3+} (f), KML:0.006Mn^{4+} (g), KML:0.02Nd^{3+} (h), and KML:0.006Mn^{4+},0.02Nd^{3+} (i). The insets are the digital luminescence photos upon a 365 nm UV lamp excitation.

$^4F_{9/2} \leftarrow {}^4I_{9/2}$, $^4S_{3/2}$, $^4F_{7/2} \leftarrow {}^4I_{9/2}$, $^4F_{5/2}$, $^2H_{9/2} \leftarrow {}^4I_{9/2}$ and $^4F_{3/2} \leftarrow {}^4I_{9/2}$, respectively.[42–45] It can be conspicuously observed that a suitable spectral overlap exists (within the blue dashed rectangle) between the PL emission spectrum of Mn^{4+} and the excitation spectrum of Nd^{3+} in Fig. 3a and b, illustrating the possibility of resonant energy transfer from Mn^{4+} to Nd^{3+} ions. Fig. 3c shows the combined excitation–emission spectra of the Mn^{4+},Nd^{3+} co-doped NML sample. In the PL emission spectrum, the characteristic emission bands of Nd^{3+} upon 365 nm UV excitation are clearly visible, in addition to the emission band of Mn^{4+}, which remains present but is strongly reduced in intensity. The excitation spectrum monitored at 1072 nm (the Nd^{3+} $^4F_{3/2} \rightarrow {}^4I_{11/2}$ emission transition) clearly contains the double Mn^{4+} excitation band with a maximum at 350 nm, illustrating that energy transfer from Mn^{4+} to Nd^{3+} ions takes place in NML:Mn^{4+},Nd^{3+} samples. Similar conditions of PL emission and excitation spectra appear in Mn^{4+},Nd^{3+} doped NMG and KML samples, which are clearly shown in Fig. S2b (ESI†), Fig. 3d–f and Fig. S2c (ESI†), Fig. 3g–i, respectively. We therefore conclude that efficient energy transfer from Mn^{4+} to

This journal is © The Royal Society of Chemistry 2018

J. Mater. Chem. C, 2018, 6, 7302–7310 | 7305

Nd^{3+} ions takes place in the as-prepared Mn^{4+},Nd^{3+} co-doped samples to effectively realize broadband conversion of UV/visible light into NIR emission.

In order to further investigate the energy transfer between Mn^{4+} and Nd^{3+}, several Mn^{4+},Nd^{3+} co-doped samples of NML:0.02Mn^{4+},xNd^{3+} (x = 0.002–0.4), NMG:0.01Mn^{4+},yNd^{3+} (y = 0.004–0.4) and KML:0.006Mn^{4+},zNd^{3+} (z = 0.002–0.4) with different Nd^{3+} concentrations were prepared. The PL emission spectra upon 365 nm excitation of the as-prepared Mn^{4+},Nd^{3+} co-doped sample series are shown in Fig. 4a, c and e. It can be observed that all the emission spectra of these Mn^{4+},Nd^{3+} co-doped samples present both Mn^{4+} and Nd^{3+} emissions upon 365 nm UV excitation. With increasing Nd^{3+} concentration x/y/z, the Mn^{4+} emission intensity decreases monotonously, whereas the emission intensity of Nd^{3+} reaches a maximum and then decreases. The optimal concentration of Nd^{3+} can be easily found from Fig. 4a, c and e with x = 0.01 in NML:0.02Mn^{4+},xNd^{3+}, y = 0.02 in NMG:0.01Mn^{4+},yNd^{3+} and z = 0.015 in KML:0.006Mn^{4+},zNd^{3+}. It is obvious that the energy transfer from Mn^{4+} to Nd^{3+} ions in this sample series is effective. Additionally, luminescence decay lifetime measurements can supply further insight into the energy transfer phenomenon. Fig. 4b, d and f give the decay curves of the Mn^{4+} emission in

Fig. 4 PL emission spectra (λ_{ex} = 365 nm) of NML:0.02Mn^{4+},xNd^{3+} (a), NMG:0.01Mn^{4+},yNd^{3+} (c), and KML:0.006Mn^{4+},zNd^{3+} (e) and the corresponding decay curves for (b) NML:0.02Mn^{4+},xNd^{3+} (λ_{ex} = 365 nm, λ_{em} = 705 nm), (d) NMG:0.01Mn^{4+},yNd^{3+} (λ_{ex} = 365 nm, λ_{em} = 697 nm), and (f) KML:0.006Mn^{4+},zNd^{3+} (λ_{ex} = 365 nm, λ_{em} = 696 nm).

NML:0.02Mn^{4+},xNd^{3+} (λ_{ex} = 365 nm, λ_{em} = 705 nm), NMG:0.01Mn^{4+},yNd^{3+} (λ_{ex} = 365 nm, λ_{em} = 697 nm), and KML: 0.006Mn^{4+},zNd^{3+} (λ_{ex} = 365 nm, λ_{em} = 696 nm) with different Nd^{3+} concentrations. All the decay curves match well with a bi-exponential function expressed as follows:[46]

$$I(t) = I_0 + A_1 \exp(-t/\tau_1) + A_2 \exp(-t/\tau_2) \quad (1)$$

where $I(t)$ and I_0 correspond to the luminescence intensities at time t and 0, respectively. Both A_1 and A_2 are constants, and τ_1 and τ_2 represent the luminescence lifetimes of the fast and slow decay components, respectively. The average decay times ($\tau^\star$) are determined via the equation below using the parameters after fitting the decay curves:[47]

$$\tau^\star = (A_1\tau_1^2 + A_2\tau_2^2)/(A_1\tau_1 + A_2\tau_2) \quad (2)$$

Accordingly, the decay times are 0.986, 0.887, 0.826, 0.729, 0.667, 0.611 and 0.561 ms corresponding to x = 0, 0.002, 0.005, 0.01, 0.02, 0.03, and 0.04 in NML:0.02Mn^{4+},xNd^{3+} (represented in Fig. 4b), 0.585, 0.484, 0.380, 0.269, 0.186 and 0.153 ms corresponding to y = 0, 0.004, 0.012, 0.02, 0.03 and 0.04 in NMG:0.01Mn^{4+},yNd^{3+} (represented in Fig. 4d), and 1.315, 1.159, 0.946, 0.807, 0.722, 0.605, 0.511 and 0.419 ms corresponding to z = 0, 0.002, 0.005, 0.01, 0.015, 0.02, 0.03 and 0.04 in KML:0.006Mn^{4+},zNd^{3+} (represented in Fig. 4e). It is obvious that the Mn^{4+} decay time decreases monotonously with increasing Nd^{3+} concentration in all these three kinds of phosphors, as listed in Table S1 (ESI†), which gives a strong confirmation for the efficient energy transfer from Mn^{4+} to Nd^{3+} ions in these samples.

In general, the energy transfer efficiency (η_T) from Mn^{4+} to Nd^{3+} ions can be estimated here using the decay time data via the following formula:[48]

$$\eta_T = 1 - \tau/\tau_0 \quad (3)$$

Simultaneously, the energy transfer probability (P_T), another parameter to illustrate the energy transfer effectiveness, can be defined by this equation:[49]

$$P_T = 1/\tau - 1/\tau_0 \quad (4)$$

Herein, the τ_0 and τ are the corresponding decay times for Mn^{4+} in the Mn^{4+} singly doped and the Mn^{4+},Nd^{3+} co-doped samples, which have been obtained above. As a result, the values of energy transfer efficiency (η_T) and energy transfer probability (P_T) for these three kinds of samples are listed in Table S1 (ESI†), which show the increase of η_T from 0.0837 to 0.4205 and P_T from 0.09434 to 0.7495 ms^{-1} corresponding to x from 0.002 to 0.04 in the NML:0.02Mn^{4+},xNd^{3+} samples, respectively, as depicted in Fig. 5a. Similarly, the η_T and P_T values increase from 0.1726 and 0.3567 ms^{-1} to 0.7385 and 4.827 ms^{-1} for the NMG:0.01Mn^{4+},yNd^{3+} samples corresponding to y from 0.004 to 0.04, respectively, as shown in Fig. 5b. Fig. 5c plots the η_T and P_T values for the KML:0.006Mn^{4+},zNd^{3+} samples, which increase from 0.1186 and 0.1024 ms^{-1} to 0.6814 and 1.6262 ms^{-1} corresponding to z from 0.002 to 0.04, respectively. It is concluded that both the η_T and P_T values increase monotonously with increasing Nd^{3+} concentration in these Mn^{4+},Nd^{3+} co-doped

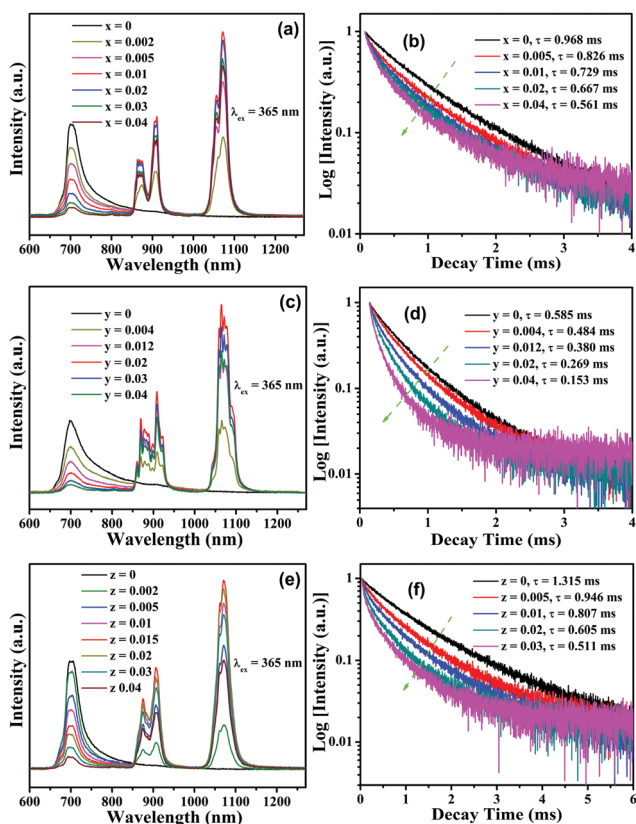7306 | J. Mater. Chem. C, 2018, 6, 7302–7310
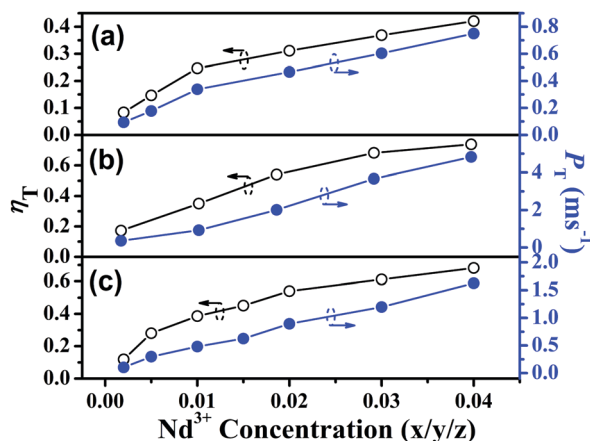
This journal is © The Royal Society of Chemistry 2018

Fig. 5 Energy transfer efficiency (η_T) and energy transfer probability (P_T) for NML:0.02Mn^{4+},xNd^{3+} (a), NMG:0.01Mn^{4+},yNd^{3+} (b) and NML: 0.006Mn^{4+},zNd^{3+} (c).

Fig. 6 Dependence of τ_0/τ of Mn^{4+} in NML:0.02Mn^{4+},Nd^{3+} (a–c), NMG:0.01Mn^{4+},Nd^{3+} (d–f) and KML:0.006Mn^{4+},Nd^{3+} (g–i) on the sum of Mn^{4+} and Nd^{3+} concentration $C^{6/3}$, $C^{8/3}$ and $C^{10/3}$.

samples with a fixed Mn^{4+} content, which illustrates that the energy transfer process becomes more and more efficient with higher Nd^{3+} concentration.

Generally, the non-radiative resonant energy transfer mechanisms include exchange interaction and electric multi-polar interactions. The critical distance (R_c) was first estimated as follows since the exchange interaction is dominant if this is less than 5 Å:[50,51]

$$R_c \approx 2 \left[\frac{3V}{4\pi X_c N} \right]^{1/3} \quad (5)$$

where V is the volume of the crystal unit cell, and N is the number of cations for dopant substitution. X_c is the total critical concentration of Mn^{4+} and Nd^{3+} at which the emission intensity of Mn^{4+} with incorporation of Nd^{3+} is half of the original intensity without Nd^{3+} in the sample series. As listed in Table 1, the volume V of the cell is 243.73(2) Å^3 for NML, 233.44(2) Å^3 for NMG and 247.70(2) Å^3 for KML, N = 3 for all three hosts, and X_c is estimated to be 0.02/2 + 0.01 = 0.02 for NML:Mn^{4+},Nd^{3+}, 0.01/2 + 0.012 = 0.017 for NMG:Mn^{4+},Nd^{3+} and 0.006/2 + 0.015 = 0.018 for KML:Mn^{4+},Nd^{3+}. Accordingly, the R_c is determined to be 19.8 Å for NML:Mn^{4+},Nd^{3+}, 20.6 Å for NMG:Mn^{4+},Nd^{3+} and 20.6 Å for KML:Mn^{4+},Nd^{3+}. Obviously, these values of R_c are much larger than 5 Å, indicating little possibility that the exchange interaction mechanism is at work here for the energy transfer from the Mn^{4+} to the Nd^{3+} ions. Therefore, it is most likely that electric multipolar interactions are responsible for the energy transfer process in these three kinds of phosphors. In view of Dexter's and Reisfeld's under-standing of energy transfer for multipolar interactions, the following formula can be used for analysis:[52–54]

$$\frac{\eta_{S0}}{\eta_S} \propto C^{\alpha/3} \quad (6)$$

where η_{S0} and η_S are the luminescence quantum efficiencies of Mn^{4+} without and with Nd^{3+} in the sample series, respectively, and C is the sum of Mn^{4+} and Nd^{3+} concentrations. α = 6, 8 and
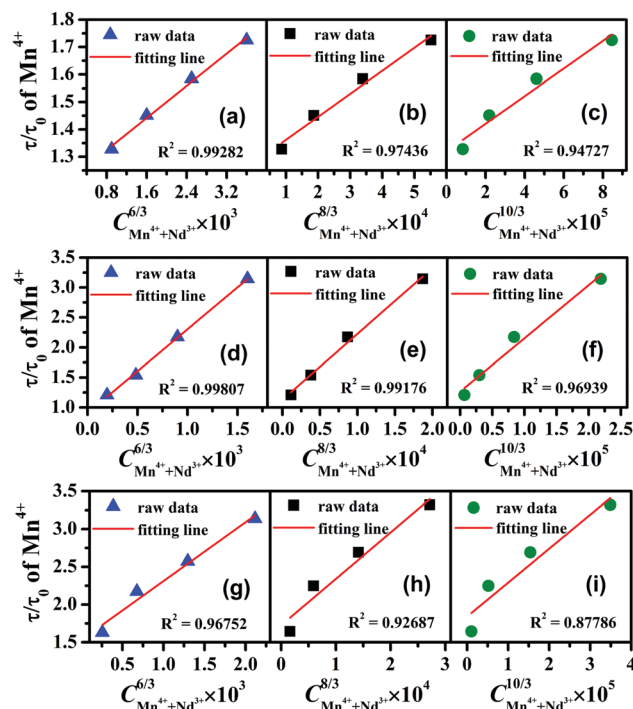
10 in eqn (6) corresponds to electric dipole–dipole, dipole–quadrupole and quadrupole–quadrupole interactions, respectively. However, the correlated lifetime ratio τ_0/τ is often used to estimate the value of η_{S0}/η_S since it is less straightforward to determine, which would convert eqn (6) into:

$$\frac{\tau_0}{\tau} \propto C^{\alpha/3} \quad (7)$$

The relationship of τ_0/τ versus $C^{\alpha/3}$ is plotted in Fig. 6a–c for NML:0.02Mn^{4+},Nd^{3+}, Fig. 6d–f for NMG:0.01Mn^{4+},Nd^{3+} and Fig. 6g–i for KML:0.006Mn^{4+},Nd^{3+}. As a consequence, all these three kinds of materials show the best fitting when α = 6 after examination of the fitting factor R, illustrating that the electric dipole–dipole interaction should mainly contribute to the energy transfer from Mn^{4+} to Nd^{3+} ions in these three kinds of materials.

In the following part, the Mn^{4+} singly doped and the Mn^{4+},Nd^{3+} co-doped samples were additionally doped with Yb^{3+} ions. Fig. 7a shows the PL excitation and emission spectra of the NML:0.02Mn^{4+},0.30Yb^{3+} sample. Upon 365 nm UV exci-tation, the emission spectrum contains both the Mn^{4+} emission band around 705 nm due to Mn^{4+} $^2E_g \rightarrow$ $^4A_{2g}$ transition, and the Yb^{3+} emission band with a maximum at around 1003 nm attributed to the Yb^{3+} $^2F_{5/2} \rightarrow$ $^2F_{7/2}$ transition. Monitored at 1003 nm, the excitation spectrum (200–900 nm) clearly con-tains the Mn^{4+} absorption band, suggesting energy transfer from Mn^{4+} to Yb^{3+} ions. Moreover, the decay time (λ_{ex} = 365 nm, λ_{em} = 705 nm) for Mn^{4+},Yb^{3+} co-doped NML:0.02Mn^{4+},0.30Yb^{3+} is much lower than that of the Mn^{4+} singly-doped NML:0.02Mn^{4+}

This journal is © The Royal Society of Chemistry 2018

J. Mater. Chem. C, 2018, 6, 7302–7310 | 7307
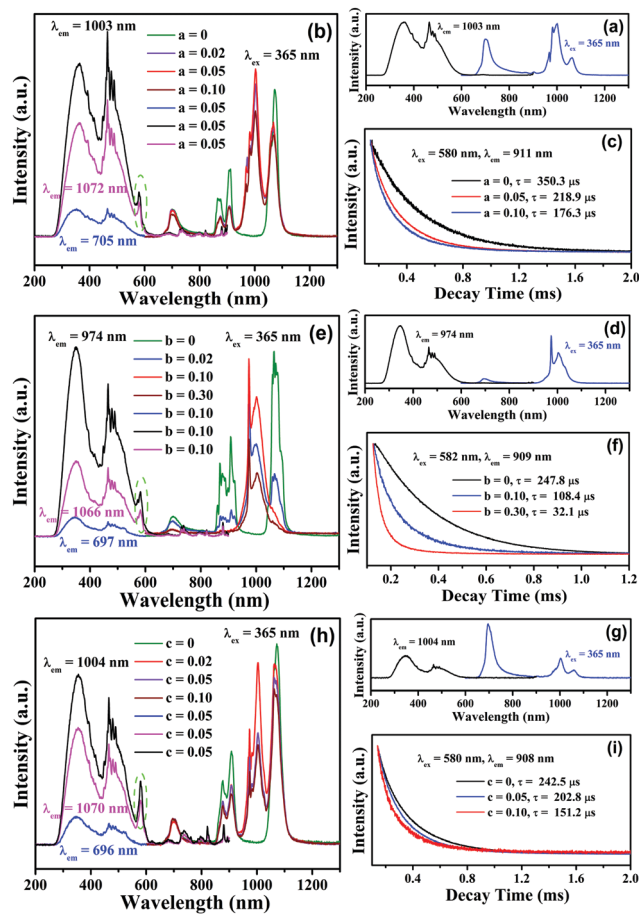
Fig. 7 PL excitation and emission spectra of (a) NML:0.02Mn^{4+},0.30Yb^{3+}, (b) NML:0.02Mn^{4+},0.01Nd^{3+},aYb^{3+}, (d) NMG:0.01Mn^{4+},0.10Yb^{3+}, (e) NMG: 0.01Mn^{4+},0.02Nd^{3+},bYb^{3+}, (g) KML:0.006Mn^{4+},0.10Yb^{3+}, and (h) KML: 0.006Mn^{4+},0.03Nd^{3+},cYb^{3+}; (c), (f) and (i) are the decay curves of NML:0.02Mn^{4+},0.01Nd^{3+},aYb^{3+} (λ_{ex} = 580 nm, λ_{em} = 911 nm), NMG:0.01Mn^{4+}, 0.02Nd^{3+},bYb^{3+} (λ_{ex} = 582 nm, λ_{em} = 909 nm), and KML:0.006Mn^{4+}, 0.03Nd^{3+},cYb^{3+} (λ_{ex} = 580 nm, λ_{em} = 908 nm), respectively.

sample, as illustrated in Fig. S3a (ESI†), further validating the energy transfer process from Mn^{4+} to Yb^{3+} ions. However, there is barely spectral overlap between the excitation spectrum of Yb^{3+} singly-doped NML:0.30Yb^{3+} in Fig. S4a (ESI†) and the emission band of Mn^{4+} singly-doped NML:0.02Mn^{4+} in Fig. 3a; thus the energy transfer process is likely to take place *via* a phonon-assisted non-resonant mechanism since there is a relatively large energy gap between the Mn^{4+} ^2E_g and Yb^{3+} $^2F_{5/2}$ levels, which requires several phonons for energy loss, as mentioned before.[32,33] Similar results are displayed in Fig. 7d, Fig. S3b, S4b (ESI†) and Fig. 3c, 7g, Fig. S4c (ESI†) for NMG:0.01Mn^{4+},0.10Yb^{3+} and KML:0.006Mn^{4+},0.10Yb^{3+}, respectively. With addition of Yb^{3+} in NML:0.02Mn^{4+},0.01Nd^{3+}, the emission spectra in Fig. 7b obviously present bands from all three ions Mn^{4+}, Nd^{3+} and Yb^{3+} in the range of 600–1300 nm upon 365 nm UV excitation. The emission intensity of Yb^{3+} increases until the Yb^{3+} concentration a = 0.05, beyond which it drops, attributed to the general concentration quenching effect, while the Nd^{3+} emission intensity decreases monotonously with

increasing Yb^{3+} concentration. This illustrates the possibility of energy transfer from Nd^{3+} to Yb^{3+} ions. Moreover, the excitation spectra monitored at the Yb^{3+} 1003 nm emission and at the Nd^{3+} 1072 nm emission are similar to that monitored at the Mn^{4+} 705 nm emission, except for the obvious characteristic Nd^{3+} excitation peak at 580 nm (indicated with a green dashed oval). Similar results have been presented in Fig. 7e and h for NMG: 0.01Mn^{4+},0.02Nd^{3+},bYb^{3+} and KML:0.006Mn^{4+},0.03Nd^{3+},cYb^{3+}, respectively, in which the optimal Yb^{3+} concentration is b = 0.10 and c = 0.02. The occurrence of this characteristic Nd^{3+} excitation line around 580 nm gives a further confirmation of the energy transfer from Nd^{3+} to Yb^{3+} ions in these co-doped Mn^{4+},Nd^{3+},Yb^{3+} samples. Moreover, the decay curves (λ_{ex} = 580 nm, λ_{em} = 911 nm) for Nd^{3+} in Fig. 7c for NML:0.02Mn^{4+}, 0.01Nd^{3+},aYb^{3+} (a = 0–0.10) are fitted well with a bi-exponential function and the decay times are calculated to be 350.3, 218.9 and 176.3 μs corresponding to a = 0, 0.05 and 0.10, respectively, which show a decrease with increasing Yb^{3+} concentration. This supplies further evidence for the energy transfer from Nd^{3+} to Yb^{3+} ions in this kind of material. The decrease of the decay times with increasing Yb^{3+} concentration in Fig. 7f (λ_{ex} = 582 nm, λ_{em} = 909 nm) and Fig. 7i (λ_{ex} = 580 nm, λ_{em} = 908 nm) analogously validates the energy transfer phenomena from Nd^{3+} to Yb^{3+} ions in NMG:0.01Mn^{4+},0.02Nd^{3+},bYb^{3+} and KML: 0.006Mn^{4+},0.03Nd^{3+},cYb^{3+}. In addition, we supply the comparison of the excitation and emission spectra of the NML:0.02Mn^{4+}, 0.02Nd^{3+},0.05Yb^{3+} material, the NMG:0.01Mn^{4+},0.02Nd^{3+},0.10Yb^{3+} sample and the KML:0.006Mn^{4+},0.03Nd^{3+},0.02Yb^{3+} sample, with the solar spectrum in Fig. 8 to show the spectral match and illustrate the possibility for spectral conversion of UV/n-UV/blue light to the NIR band for solar energy utilization. It can be seen that the excitation spectra match well with the solar spectrum in the UV and visible regions, and the emission bands are located at the ideal 930–1100 nm region for excellent response for c-Si solar energy cells. This indicates that effective broadband spectral conversion of UV/visible light to the NIR band and spectral tuning have been realized utilizing the energy transfer processes from Mn^{4+} to
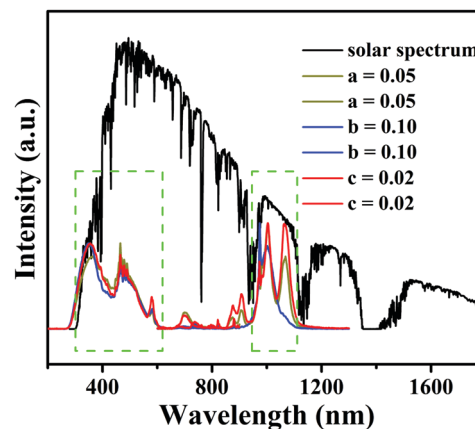
Fig. 8 Solar spectrum and PL excitation and emission spectra of NML:0.02Mn^{4+},0.01Nd^{3+},aYb^{3+}, NMG:0.01Mn^{4+},0.02Nd^{3+},bYb^{3+} and KML:0.006Mn^{4+},0.03Nd^{3+},cYb^{3+}.

7308 | J. Mater. Chem. C, 2018, 6, 7302–7310

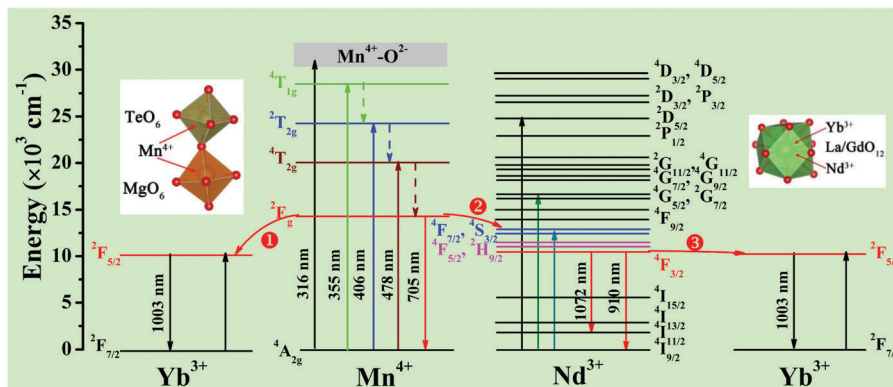This journal is © The Royal Society of Chemistry 2018

Fig. 9   Partial coordination environment in an NML structure and a schematic energy-level diagram illustrating possible energy transfer processes in NML:Mn^{4+},Nd^{3+},Yb^{3+} materials.

Nd^{3+} and then to Yb^{3+} ions in $(Na,K)Mg(La,Gd)TeO_6$:Mn^{4+},Nd^{3+},Yb^{3+} materials, which is an attractive way for spectral conversion and adjustment for NIR materials applied in solar cells, optical telecommunication, biomedical optical imaging, optical sensors *etc.*

Fig. 9 shows an overview of the partial electronic energy level diagram of NML and a schematic diagram illustrating the possible energy transfer processes occurring in NML:Mn^{4+},Nd^{3+},Yb^{3+} materials to act as an example for $(Na,K)Mg(La,Gd)TeO_6$:Mn^{4+},Nd^{3+},Yb^{3+}. As seen in Fig. 9, Mn^{4+} occupies Te^{6+} and Mg^{2+} sites with six O^{2-} coordination simultaneously to generate a red emission band around 705 nm attributed to the Mn^{4+} $^2E_g \rightarrow {}^4A_{2g}$ transition upon excitation with UV/n-UV/blue light. The energy difference between the Mn^{4+} lowest excited energy level ^2E_g (14 184 cm^{-1}) and the Yb^{3+} excited state $^2F_{5/2}$ (9970 cm^{-1}) is about 4214 cm^{-1}. When Mn^{4+} absorbs the UV/n-UV/blue excitation light, an electron is promoted to the corresponding excited states and will then relax non-radiatively to the Mn^{4+} ^2E_g level, from which it falls back to the ground state to generate red emission. The energy of the ^2E_g level is less than twice that of an Yb^{3+} phonon. Therefore, one electron can only be converted into one Yb^{3+} phonon according to a phonon-assisted non-resonant energy transfer process from Mn^{4+} to Yb^{3+} ions (step ❶) to produce an Yb^{3+} emission band around 1003 nm. It is likely that Yb^{3+} and Nd^{3+} would like to replace La/Gd sites with twelve O^{2-} around because of their similar ionic radii, as illustrated in Fig. 9. The Mn^{4+} emission band around 705 nm matches well with one excitation band of Nd^{3+}, which is a required condition for the occurrence of resonant energy transfer. Therefore, the energy at the Mn^{4+} excited state ^2E_g can be transferred to the Nd^{3+} levels $^4F_{7/2}$, $^4S_{3/2}$ *via* the Forster's Resonant Energy Transfer process to produce the 910 and 1072 nm emissions of Nd^{3+} (step ❷), which results in the decrease of the Mn^{4+} emission intensity and enhancement of the Nd^{3+} emission upon excitation in the Mn^{4+} excitation bands. In the Mn^{4+},Nd^{3+},Yb^{3+} co-doped conditions, the excited $^4F_{7/2}$, $^4S_{3/2}$ Nd^{3+} energy levels can relax non-radiatively to the $^4F_{5/2}$, $^2H_{9/2}$ Nd^{3+} energy levels, after which energy can be transferred to the $^2F_{5/2}$ Yb^{3+} excited state, to enhance Yb^{3+} emission (step ❸).

4. Conclusions

A series of $(Na,K)Mg(La,Gd)TeO_6$:Mn^{4+},Nd^{3+},Yb^{3+} materials were synthesized *via* a high-temperature solid-state reaction method. We observed that Mn^{4+} singly doped samples presented bright red luminescence under a 365 nm UV lamp excitation, due to an emission band around 700 nm attributed to the $^2E_g \rightarrow {}^4A_{2g}$ Mn^{4+} transition. When Nd^{3+} ions were co-doped into these Mn^{4+} singly doped samples, energy was transferred from Mn^{4+} to Nd^{3+} ions, based on the spectral overlap between Mn^{4+} emission and Nd^{3+} excitation. This was verified by comparing the excitation spectra monitored at the Mn^{4+} and Nd^{3+} emission bands in the Mn^{4+},Nd^{3+} co-doped samples to those of the Mn^{4+} singly doped samples. In addition, variations in the emission spectra and decreases of the Mn^{4+} decay times with increasing Nd^{3+} concentrations in the Mn^{4+},Nd^{3+} co-doped samples confirmed this principle. In view of the reported energy transfer from Nd^{3+} to Yb^{3+} ions, Yb^{3+} ions were added into the Mn^{4+},Nd^{3+} co-doped samples to illustrate the energy transfer process from Mn^{4+} to Nd^{3+} and then to Yb^{3+}, which was proved *via* the spectral and decay times analysis. Therefore, converting UV/visible light to NIR emission with better spectral response for c-Si solar cells was effectively realized *via* this kind of Mn^{4+}–Nd^{3+}–Yb^{3+} energy transfer system, which is an elegant way to enhance the energy conversion efficiency in c-Si solar cells.

Conflicts of interest

The authors have no conflicts of interest to declare.

Acknowledgements

References

1 B. M. Van Der Ende, L. Aarts and A. Meijerink, *Phys. Chem. Chem. Phys.*, 2009, **11**, 11081–11095.

2 J. Liu, Y. Yao, S. Xiao and X. Gu, *J. Phys. D: Appl. Phys.*, 2018, **51**, 123001.

3 M. Neukom, S. Züfle, S. Jenatsch and B. Ruhstaller, *Sci. Technol. Adv. Mater.*, 2018, **19**, 291–316.

4 M. Yamaguchi, K.-H. Lee, K. Araki and N. Kojima, *J. Phys. D: Appl. Phys.*, 2018, **51**, 133002.

5 B. Richards, *Sol. Energy Mater. Sol. Cells*, 2006, **90**, 1189–1207.

6 T. Trupke, M. Green and P. Würfel, *J. Appl. Phys.*, 2002, **92**, 1668–1674.

7 S. Kalytchuk, S. Gupta, O. Zhovtiuk, A. Vaneski, S. V. Kershaw, H. Fu, Z. Fan, E. C. H. Kwok, C.-F. Wang, W. Y. Teoh and A. L. Rogach, *J. Phys. Chem. C*, 2014, **118**(30), 16393–16400.

8 X. Huang, S. Han, W. Huang and X. Liu, *Chem. Soc. Rev.*, 2013, **42**, 173–201.

9 B. M. van der Ende, L. Aarts and A. Meijerink, *Adv. Mater.*, 2009, **21**(30), 3073–3077.

10 J. Chen, J. Liu, H. Yin, S. Jiang, H. Yao and X. Yu, *J. Am. Ceram. Soc.*, 2016, **99**(1), 141–145.

11 Q. Y. Zhang and X. Y. Huang, *Procedia Mater. Sci.*, 2010, **55**, 353–427.

12 K. Yoshikawa, H. Kawasaki, W. Yoshida, T. Irie, K. Konishi, K. Nakano, T. Uto, D. Adachi, M. Kanematsu, H. Uzu and K. Yamamoto, *Nat. Energy*, 2017, **2**, 17032.

13 P. Cheng, Y. Zhou, X. Su, M. Zhou, Z. Zhou and H. Shao, *J. Lumin.*, 2018, **197**, 31–37.

14 D. C. Yu, X. Y. Huang, S. Ye, M. Y. Peng and Q. Y. Zhang, *Sol. Energy Mater. Sol. Cells*, 2012, **101**, 303–307.

15 M. Olfa, J. Merigeon, B. Boulard and M. Girtan, *Opt. Mater.*, 2016, **60**, 235–239.

16 Y. Li, S. Zhou, H. Lin, X. Hou and W. Li, *Opt. Mater.*, 2010, **32**(9), 1223–1226.

17 F. Huang, L. Chen, Y. Han, J. Tang, Q. Nie, P. Zhang and Y. Xu, *Infrared Phys. Technol.*, 2015, **71**, 159–162.

18 J. Li, L. Chen, Z. Hao, X. Zhang, L. Zhang, Y. Luo and J. Zhang, *Inorg. Chem.*, 2015, **54**, 4806–4810.

19 M. Y. A. Yagoub, H. C. Swart, M. S. Dhlamini and E. Coetsee, *Opt. Mater.*, 2016, **60**, 521–525.

20 T. Yu, D. C. Yu, H. H. Lin and Q. Y. Zhang, *J. Alloys Compd.*, 2017, **695**, 1154–1159.

21 R. Zhou, Y. Kou, X. Wei, Y. Chen and M. Yin, *Appl. Phys. B: Lasers Opt.*, 2012, **107**(2), 483–487.

22 S. Ye, J. Zhou, S. Wang, R. Hu, D. Wang and J. Qiu, *Opt. Express*, 2013, **21**, 4167–4173.

23 Y. Teng, J. Zhou, X. Liu, S. Ye and J. Qiu, *Opt. Express*, 2015, **18**, 9671–9676.

24 T. Sun, X. Chen, L. Jin, H.-W. Li, B. Chen, B. Fan, B. Moine, X. Qiao, X. Fan, S.-W. Tsang, S. F. Yu and F. Wang, *J. Phys. Chem. Lett.*, 2017, **8**, 5099–5104.

25 M. N. Getz, P.-A.s Hansen, Ø. S. Fjellvåg, M. A. K. Ahmed, H. Fjellvåg and O. Nilsen, *J. Mater. Chem. C*, 2017, **5**, 8572–8578.

26 R. A. Talewar, C. P. Joshi and S. V. Moharil, *J. Lumin.*, 2018, **197**, 1–6.

27 F. Qu and N. O. Dantas, *Physica B*, 2003, **327**(1), 79–87.

28 M. G. Brik, S. J. Camardello and A. M. Srivastava, *ECS J. Solid State Sci. Technol.*, 2015, **4**(3), R39–R43.

29 W. Lü, M. Jiao, B. Shao, L. Zhao, Y. Feng and H. You, *Dalton Trans.*, 2016, **45**, 466–468.

30 W. Li, T. Chen, W. Xia, X. Yang and S. Xiao, *J. Lumin.*, 2018, **194**, 547–550.

31 J. Xiang, J. Chen, N. Zhang, H. Yao and C. Guo, *Dyes Pigm.*, 2018, **154**, 257–262.

32 S. Ye, J. Zhou, S. Wang, R. Hu, D. Wang and J. Qiu, *Opt. Express*, 2013, **21**(4), 4167–4173.

33 D. Ghosh, S. Balaji, K. Biswas and K. Annapurna, *J. Appl. Phys.*, 2016, **120**, 233104.

34 D. Chen, Y. Yu, H. Lin, P. Huang, Z. Shan and Y. Wang, *Opt. Lett.*, 2010, **35**, 220–222.

35 F. J. Pedraza, C. Rightsell, G. A. Kumar, J. Giuliani, C. Monton and D. K. Sardar, *Appl. Phys. Lett.*, 2017, **110**, 223107.

36 F. Liegard, J. L. Doualan, R. Moncorge and M. Bettinelli, *Appl. Phys. B: Lasers Opt.*, 2005, **80**, 985–991.

37 L. Liu, M. Li, S. Cai, Y. Yang and Y. Mai, *Opt. Mater. Express*, 2015, **5**, 756–763.

38 K. Li, H. Lian and R. Van Deun, *J. Lumin.*, 2018, **198**, 155–162.

39 K. Li, H. Lian and R. Van Deun, *Dalton Trans.*, 2018, **47**, 2501–2505.

40 C. Larson and R. B. Von Dreele, Generalized Structure Analysis System (GSAS), Los Alamos National Laboratory Report LAUR, 86 Los Alamos National Laboratory, Los Alamos, NM, 1994, p. 748.

41 J.-F. Wyart, A. Meftah, A. Bachelier, J. Sinzelle, W.-Ü. Lydia Tchang-Brillet, N. Champion, N. Spector and J. Sugar, *J. Phys. B: At., Mol. Opt. Phys.*, 2006, **39**, L77–L82.

42 J.-M. Meijer, L. Aarts, B. M. van der Ende, T. J. H. Vlugt and A. Meijerink, *Phys. Rev. B: Condens. Matter Mater. Phys.*, 2010, **81**, 035107.

43 Y. Yu, Y. Huang, L. Zhang, Z. Lin and G. Wang, *J. Alloys Compd.*, 2015, **651**, 164–169.

44 R. Bazzi, A. Brenier, P. Perriat and O. Tillement, *J. Lumin.*, 2005, **113**, 161–167.

45 W. T. Carnall, P. R. Fields and K. Rajnak, *J. Chem. Phys.*, 1968, **49**, 4424–4442.

46 H. Zhou, Y. Jin, M. Jiang, Q. Wang and X. Jiang, *Dalton Trans.*, 2015, **44**, 1102–1109.

47 Q. Guo, Q. Wang, L. Jiang, L. Liao, H. Liu and L. Mei, *Phys. Chem. Chem. Phys.*, 2016, **18**, 15545–15554.

48 P. I. Paulose, G. Jose, V. Thomas, N. V. Unnikrishnan and M. K. R. Warrier, *J. Phys. Chem. Solids*, 2003, **64**, 841–846.

49 C. Liu, D. Hou, J. Yan, L. Zhou, X. Kuang, H. Liang, Y. Huang, B. Zhang and Y. Tao, *J. Phys. Chem. C*, 2014, **118**, 3220–3229.

50 Y. Jin, Y. Hu, H. Wu, H. Duan, L. Chen, Y. Fu, G. Ju, Z. Mu and M. He, *Chem. Eng. J.*, 2016, **288**, 596–607.

51 G. Blasse, *Philips Res. Rep.*, 1969, **24**, 131–144.

52 D. L. Dexter, *J. Chem. Phys.*, 1953, **21**, 836–850.

53 R. Reisfeld and N. Lieblich-Soffer, *J. Solid State Chem.*, 1979, **28**, 391–395.

54 M. Shang, S. Liang, H. Lian and J. Lin, *Inorg. Chem.*, 2017, **56**, 6131–6140.

7310 | *J. Mater. Chem. C*, 2018, **6**, 7302–7310

This journal is © The Royal Society of Chemistry 2018